



RESEARCH ARTICLE

10.1029/2018JD030141

Drizzle and Turbulence Below Closed Cellular Marine Stratocumulus Clouds

Virendra P. Ghate¹ and Maria P. Cadetdu¹ ¹Argonne National Laboratory, Lemont, IL, USA

Key Points:

- On average the drizzle shafts are 28.14 km wide, with cloud base rain rate and modal diameter of 1.26 mm/day and 145.26 micron
- The average diabatic cooling due to drizzle evaporation is -30.60 W/m^2 in the subcloud layer
- For similar amount of radiative cooling at the cloud top, drizzle evaporation decreases below cloud turbulence by about 16%

Supporting Information:

- Supporting Information S1

Correspondence to:

V. P. Ghate,
vghate@anl.gov

Citation:

Ghate, V. P., & Cadetdu, M. P. (2019). Drizzle and turbulence below closed cellular marine stratocumulus clouds. *Journal of Geophysical Research: Atmospheres*, 124, 5724–5737. <https://doi.org/10.1029/2018JD030141>

Received 10 DEC 2018

Accepted 19 APR 2019

Accepted article online 2 MAY 2019

Published online 4 JUN 2019

Author Contributions:

Formal analysis: Virendra P. Ghate, Maria P. Cadetdu**Methodology:** Virendra P. Ghate, Maria P. Cadetdu**Writing - original draft:** Virendra P. Ghate, Maria P. Cadetdu**Writing - review & editing:** Virendra P. Ghate, Maria P. Cadetdu

Abstract Drizzle is ubiquitous in marine boundary layer stratocumulus clouds with much of it evaporating before reaching the surface. Ten days of observations made at the Atmospheric Radiation Measurement's Eastern North Atlantic site during closed cellular stratocumulus cloud conditions are used to characterize drizzle below the cloud base and its impact on the boundary layer turbulence. Cloud and drizzle microphysical and macrophysical properties were retrieved by combining the data from vertically pointing Doppler cloud radar, ceilometer, and microwave radiometer. On average, the drizzle shafts were 28.14 km wide, with cloud base rain rate and modal diameter of 0.98 mm/day and $138.62 \mu\text{m}$, respectively. The rain rate at the surface was negligible yielding an average diabatic cooling of -28.68 W/m^2 in the subcloud layer. The liquid water path and turbulence within the boundary layer increased with an increase in the cloud top radiative cooling; however, none of these variables exhibited any relationship with cloud base rain rate. For a similar amount of radiative cooling at the cloud top, the average variance of vertical velocity in the subcloud layer was about 16% lower during strongly precipitating conditions as compared to lightly precipitating conditions. The reduction in the variance of vertical velocity due to drizzle evaporation was primarily confined to the upper half of the subcloud layer and was due to reduction in the strengths of the downdrafts. Collectively, our results show substantial impact of drizzle evaporation on turbulence below stratocumulus clouds, necessitating its accurate representation in the Earth system models.

1. Introduction

Marine boundary layer stratocumulus clouds cover vast areas of Eastern subtropical oceans and persist for long timescales (Klein & Hartmann, 1993). These clouds reflect greater amount of solar radiation back to space compared to the ocean surface, causing net cooling of the Earth's surface. Hence, these clouds are an important component of the Earth's radiation budget and need to be accurately represented in the Earth system models (ESMs) aimed at predicting the future climate. Stratocumulus clouds are intimately coupled to the turbulence in the boundary layer that is primarily maintained by radiative cooling at the cloud top and is modulated by entrainment, surface turbulent fluxes, wind shear, and precipitation (Wood, 2012). Precipitation is known to be ubiquitous in these clouds with much of it evaporating before reaching the surface (Wood et al., 2015; Zhou et al., 2015 etc.). Marine boundary layer stratocumulus clouds occur in distinct mesoscale organizations named closed cellular (completely overcast) and open cellular (Sharon et al., 2006; Stevens et al., 2005), with precipitation being one of the key factors causing boundary layer decoupling and the transition between these organizations (Feingold et al., 2015; Rapp, 2016; Yamaguchi et al., 2017).

Several parameterizations have been proposed to represent stratocumulus clouds in ESM as they occur at spatial scales smaller than the model grid spacing. The most sophisticated parameterizations use higher-order moments of the joint probability distribution functions of total water mixing ratio, liquid water potential temperature, and vertical air motion (e.g., Bogenschutz et al., 2013; Golaz et al., 2002). Recently, there have been attempts to represent these clouds in the ESM in a unified way by coupling these higher-order cloud schemes to bin microphysics schemes (Gettelman & Morrison, 2015; Morrison & Gettelman, 2008). The model simulations made in such a setup showed a stable cold moist layer near the surface caused by evaporation of the drizzle in the subsaturated subcloud layer. This stable layer inhibited replenishing of cloud water by shutting off boundary layer turbulence thereby causing spurious oscillations in cloud cover (Zheng et al., 2016, 2017). These and other studies have called for observational studies that quantify and characterize drizzle and its evaporation in these systems and assess the impact of drizzle evaporation-induced cooling on the boundary layer turbulence (Ahlgriem & Forbes, 2014; Wood et al., 2016).

©2019. The Authors.

This is an open access article under the terms of the Creative Commons Attribution-NonCommercial-NoDerivs License, which permits use and distribution in any medium, provided the original work is properly cited, the use is non-commercial and no modifications or adaptations are made.

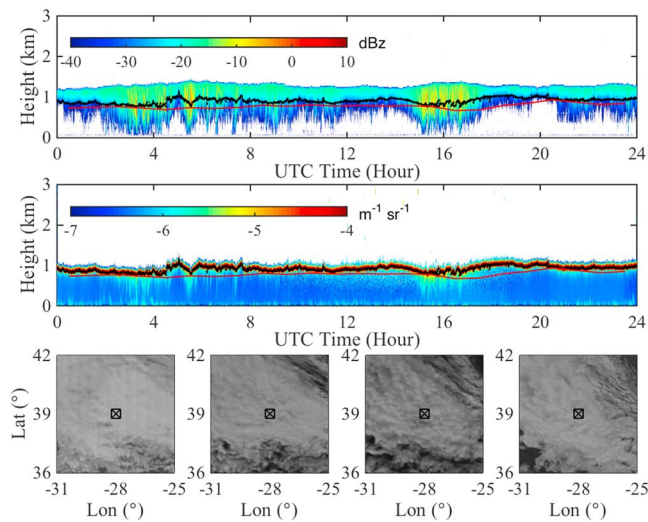


Figure 1. (top) Time-height profile of Ka-band Atmospheric Radiation Measurement Zenith Radar reflectivity (shades), ceilometer cloud base height (black line), and lifting condensation level (red). (middle) Time-height profile of ceilometer-reported backscatter (shades), cloud base height (black line), and lifting condensation level (red line). (lower) Visible satellite imagery captured by Spinning Enhanced Visible and Infrared Imager at 10, 13, 16, and 19 UTC (from left to right). The case was observed on 4 March 2016.

In this study, we have used observations collected at the Atmospheric Radiation Measurement (ARM)'s Eastern North Atlantic (ENA) site during closed cellular (Figure 1) stratocumulus cloud conditions to address this need. The data and retrieval techniques are described in the next section, followed by sections that describe the average boundary layer and drizzle properties. The impact of drizzle evaporation on turbulence structure is reported in section 5. The article is concluded with a section 6.

2. Data and Methodology

2.1. Instrumentation and Radiative Transfer Model

The ARM ENA site is located on the Northern point of the Graciosa island (39°N, 28°W, 15 MSL). It has several instruments to make detailed measurements of aerosol, cloud, precipitation, and dynamic and thermodynamic fields (Wood et al., 2015). Discussed here are only the instruments used in the study. A vertically pointing Ka-band Doppler cloud radar operating at 35-GHz frequency (Ka-band ARM Zenith Radar [KAZR]) records the raw Doppler spectrum and its first three moments in copolarization and cross-polarization at a 2-s temporal and 30-m range resolutions. The data from copolarized mode only were used in this study. The KAZR was calibrated by comparing it with the Ka-band Scanning ARM Cloud Radar that is calibrated using a corner reflector. Hence, the KAZR calibration is accurate within 1 dB. A laser ceilometer operating at 905-nm wavelength was collocated to the KAZR and recorded the raw backscatter and the first three optical cloud base heights

at a 15-s temporal and 30-m range resolution. A three-channel microwave radiometer (MWR) recorded the brightness temperatures at 23.8, 31.4, and 90 GHz at a 10-s temporal resolution, which can be used to retrieve the column integrated water vapor (IWV) and liquid water path (LWP). The MWR is continuously calibrated using tip curves (Cadeddu et al., 2013). A Doppler lidar that operates at 1.5- μm wavelength is also present at the site and records the backscatter and Doppler velocity at a 1-s temporal and 30-m range resolution. Surface meteorological instruments recorded surface air temperature, humidity, pressure, and winds at 1-min temporal resolution. Radiosondes are launched at the site twice daily at 00 and 1200 UTC, and they provide profiles of temperature, moisture, pressure, and winds. Visible satellite imagery around the site location from the Spinning Enhanced Visible and Infrared Imager onboard the Meteosat Second Generation satellite were also used.

The sea surface temperature (SST) used in this study was taken from the hourly output of the European Center for Medium-range Weather Forecasting (ECMWF) reanalysis model at the grid box over the ocean closest to the site. Cloud boundaries were retrieved using the technique by Clothiaux et al. (2000). Due to the influence of land on the surface meteorological data, we calculated the lifting condensation level (LCL) using the ECMWF reported SST and the water vapor mixing ratio from the meteorological tower per formulation by Bolton (1980). Such a calculation of LCL assumes the impact of land surface on the humidity to be minimal and the LCL to be primarily controlled by the SST. For the simulation of profiles of radiative fluxes and heating rates, the Rapid Radiative Transfer Model (RRTM; Iacono et al., 2000; Morcrette et al., 2001) was used at a minute temporal resolution and 20-m vertical resolution. The interpolated sondes data product (Toto & Jensen, 2016) available from the ARM archive were used as an input to the radiative transfer model. The setup and input to the RRTM was similar to that used by Ghatge et al. (2015, 2016) with the addition of the profiles of derived drizzle microphysical properties. The radiative cooling at the cloud top was calculated by subtracting the net radiative flux 40 m below the cloud top from the flux 40 m above the cloud top.

2.2. Drizzle Properties Retrieval

Prior to performing the drizzle property retrievals, it was necessary to clean and calibrate the ceilometer data. The ceilometer data were filtered for noise using the technique proposed by Kottahaus et al. (2016) and calibrated using the technique proposed by O'Connor et al. (2004). Details of the ceilometer

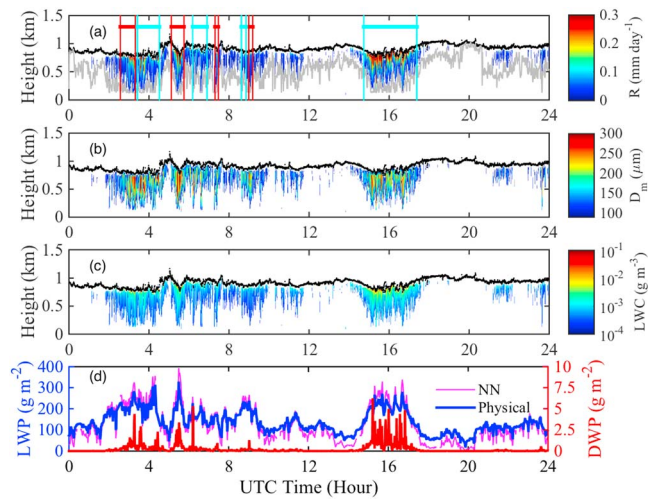


Figure 2. Time-height profiles of retrieved drizzle (a) rain rate, (b) modal diameter, and (c) liquid water content (LWC) along with the ceilometer cloud base height (black). Also shown in panel (a) is the height of the lowest Ka-band ARM Zenith Radar-reported echo (gray), the start and end of drizzle shafts (vertical bars), and the width of drizzle shafts (horizontal bars). (d) Time series of liquid water path (LWP) calculated using the neural network (NN) algorithm (magenta), LWP from physical algorithm (blue), and below-cloud drizzle water path (DWP; red). The retrievals are for the same day (4 March 2016) shown in Figure 1.

calibration procedure are described in Appendix A. The calibrated ceilometer backscatter and the KAZR reported that first three moments of Doppler spectra were used to retrieve profiles of drizzle microphysical properties below the cloud base at 1-min temporal and 30-m range resolution using the technique proposed by O'Connor et al. (2005). Briefly, the technique exploits the fact that (i) the ratio of radar reflectivity (Z) to ceilometer backscatter (β) is proportional to the fourth power of modal diameter, and (ii) after accounting for contributions from turbulence, finite beam width, and wind shear, the width of the Doppler spectra (σ) represents contribution only from the drop size distribution (DSD). Drizzle is assumed to have a three-parameter normalized gamma DSD (Testud et al., 2001), and iterations are performed between two equations to calculate the profiles of modal diameter (D_m), shape parameter (μ), and number concentration (N). From D_m , μ , and N , the profiles of drizzle liquid water content (LWC), rain rate (RR), and below cloud drizzle water path (DWP) were calculated. The overall uncertainty is 14% in the D_m , 10% in the LWC, and 20% in the RR. Further details on the technique and the complete set of equations can be found in O'Connor et al. (2005).

Profiles of drizzle modal diameter, LWC, and RRs retrieved for 4 March 2016 are shown in Figure 2. The gray lines in Figure 2a represent the height of the lowest KAZR-reported echo. It can be seen that the retrievals are only valid when RRs are strong enough to be detectable by the radar as well as the ceilometer. Two main factors determine the availability of the

retrievals: (i) The retrieval algorithm assumes a diameter-fall velocity relationship (Gossard et al., 1990; Frisch et al., 1995) that is only valid for drops larger than 90 microns in diameter, thereby dictating the minimum drop size for this technique, and (ii) the ceilometer backscatter from weak drizzle is not significantly higher than the background aerosol backscatter, for example, in Figure 1 between 10:00–14:00 and 20:00–24:00 UTC. This issue is discussed further in the next section and in the discussion section. The retrieved RRs, modal diameter, and LWC were consistent with estimates from previous studies that used remote sensing observations (Borque et al., 2018; Luke & Kollias, 2013) and aircraft observations (Stevens, Lenschow, Faloona, et al., 2003; Stevens, Lenschow, Vali, et al., 2003; Wood, 2005).

2.3. LWP Retrievals

Microwave radiometers provide sky brightness temperature measurements that in turn depend on the atmospheric IWV and liquid water. Traditional retrievals employ a variety of inversion techniques to retrieve IWV and LWP from microwave measurements (e.g., Liljegren et al., 2001). During heavy precipitating conditions, measurements are affected by the deposition of liquid water on the instrument's window, and LWP cannot be derived. Under light-precipitating conditions, however, the instrument's dew-blower and heater are sufficient to keep the brightness temperature measurements free of water deposition contamination. For MWRs operating at frequency of 90 GHz or above, the presence of larger droplets ($D_m > 100 \mu\text{m}$) below and within the cloud can affect the measurements by introducing unaccounted scattering effects. Cadeddu et al. (2017) found that neglecting the scattering effects by larger hydrometeors can lead to an overestimation of the column LWP. In this work, we build on those findings and combine the retrieved profiles of D_m and LWC, with the microwave brightness temperatures from the MWR to retrieve column water vapor and liquid water using a technique that accounts for scattering from precipitating hydrometeors. The details of the LWP optimal estimation scheme, hereafter called "physical retrieval," are provided in Appendix B. The uncertainty in the retrieved LWP using the physical retrieval generally varies between 7 and 15 g/m^2 .

The first guess estimates of LWP provided with the data files are derived using a neural network (NN) technique that assumes nonscattering conditions. The uncertainty for the NN retrieval, expressed as a root mean square error, can be found in the data file and is $\sim 20 \text{ g}/\text{m}^2$. Shown in Figure 2d is the LWP retrieved from the MWR3C with the physical (blue line) and NN (magenta line) algorithm. During precipitation, the retrieved LWP is generally less than the first guess because of scattering effects. Apart from the differences during

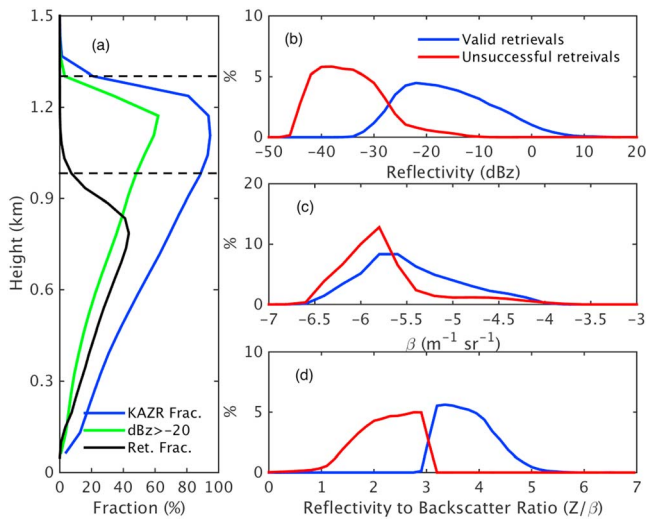


Figure 3. (a) Average profiles of Ka-band Atmospheric Radiation Measurement Zenith Radar (KAZR) hourly echo fraction (blue), hourly fraction of KAZR reflectivity greater than -20 dBz (green), and retrieval fraction (black). The horizontal dashed lines denote average cloud boundaries. (b) Histogram of radar reflectivity below cloud base, (c) histogram of ceilometer backscatter below cloud base, and (d) histogram of ratio of radar reflectivity to ceilometer backscatter below cloud base. The blue and red lines in panels b, c, and d represent samples with valid retrievals and samples that had unsuccessful retrievals, respectively.

from Doppler lidar were used to calculate hourly profiles of variance and skewness of vertical velocity and average strength of updrafts and downdrafts below the cloud base. The hourly averaged vertical profiles of radiative fluxes and heating rates were normalized with respect to the cloud top height, and the vertical profiles of hourly averaged drizzle microphysical and boundary layer turbulence properties were normalized with respect to the cloud base height for further analysis. Twenty-four out of the 240 hr of data were removed due to various reasons such as presence of shallow cumulus clouds below stratocumulus, instrument clutter, and malfunction, resulting in 216 hr of usable data.

3.1. Retrieval Efficacy

Before the retrieval results are presented it is useful to put in perspective the general retrieval methodology. The blue line in Figure 3a shows the percent of hourly KAZR valid echoes at each gate. The green and black lines represent the percentage of echoes stronger than -20 dBz and those from which retrievals were derived, respectively. The average ceilometer hourly cloud fraction for the 216 hr was 96%, and the hourly fraction of time when the column maximum reflectivity was greater than -20 dBz was 75%. The profiles in Figure 3a are consistent with a scenario of precipitating stratocumulus clouds with $\sim 100\%$ cloudiness and less than 10% precipitation reaching the surface. The fraction of samples with reflectivity greater than -20 dBz (green line) is $\sim 60\%$ in the cloud layer and $\sim 40\%$ near the cloud base. Looking at the fraction of valid retrievals (black line), one can see that it peaks well below the cloud base and is slightly higher than the fraction of samples with reflectivity greater than -20 dBz. This confirms the presence of drizzle drops even for radar reflectivity values much lower than -20 dBz, a widely used threshold for identifying drizzle.

The distribution of radar reflectivity, ceilometer backscatter, and the ratio of the two below the cloud base are shown in Figures 3b, 3c, and 3d, where the blue and red lines refer to samples with valid drizzle retrievals and samples for which drizzles retrievals were unsuccessful, respectively. Similar figure with cumulative distribution function is included in the supporting information. The distribution of ceilometer backscatter was similar for “valid” and “unsuccessful” retrievals, while the probability distribution function of radar reflectivity presented a fairly distinct range of reflectivity for the two distributions, approximately between -32 and 10 dBz for samples with valid retrievals, and between -45 and -20 dBz for samples with unsuccessful retrievals. The ratio of the reflectivity to backscatter exhibited a clear distinction (at $3 \text{ mm}^6 \cdot \text{m}^{-2} \cdot \text{Sr}$) between

precipitation the two retrievals present differences even in nonprecipitating conditions. This is expected as the NN is a statistical methodology, while the physical retrieval requires the algorithm to converge and the LWP to be consistent with the radiation measurements within a specified error. In addition, the two retrievals utilize different radiative transfer models. In nonprecipitating conditions, the two retrievals generally agree within their respective uncertainties. The DWP below cloud base derived from the KAZR-ceilometer technique is shown in red. Notice the different scales on the left and right axis for the total and drizzle LWP showing that the drizzle LWP is generally much less than 5% of the total LWP. LWP retrieved using the physical retrieval is used in the rest of the analysis.

3. General Conditions

The retrieval technique was applied to 10 cases of closed cellular marine stratocumulus clouds observed at the ARM ENA site. The 10 days were selected based on the following conditions: had over 90% cloud cover below 3 km based on the KAZR and ceilometer data, were devoid of heavy precipitate, had cloud top temperature above 0°C , and had northerly wind conditions. The case selection criteria were applied to 2 years of data from summer 2015 to summer 2017. In addition, Spinning Enhanced Visible and Infrared Imager visible images were used to confirm completely overcast conditions around the site. The derived cloud boundaries, retrieved cloud and drizzle macrophysical properties, profiles of radiative fluxes and heating rates, and the profiles of drizzle microphysical properties were averaged to hourly timescales. After filtering for noise, the data

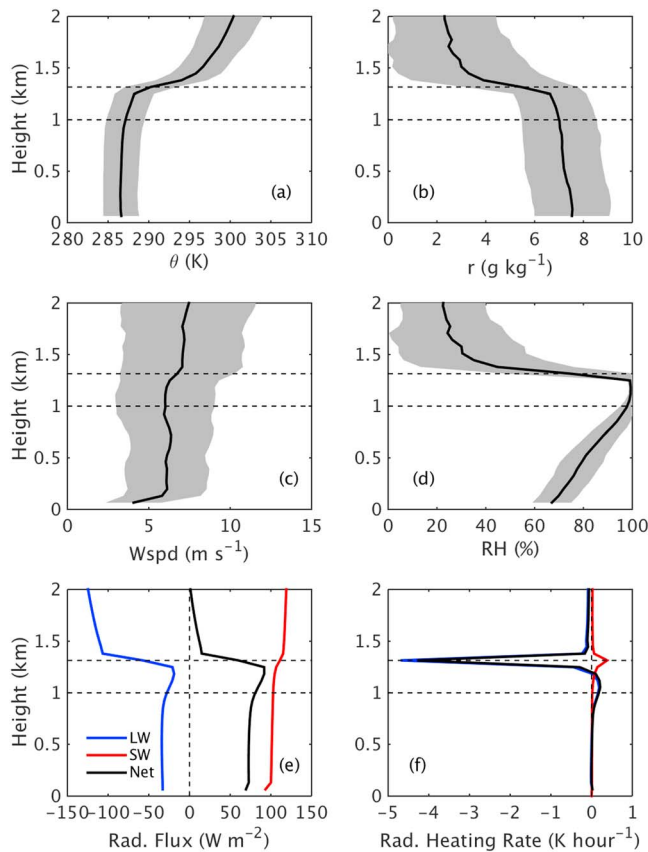


Figure 4. Average profiles of potential temperature (a), water vapor mixing ratio (b), wind speed (c), and relative humidity (RH; d) from the 22 radiosonde launches. The shades represent the one standard deviation values from the mean. Average profiles of longwave (LW), shortwave (SW), and net radiative fluxes (e) and radiative heating rates (f) from the Rapid Radiative Transfer Model simulations. The horizontal dashed lines in all panels show the average cloud boundaries.

samples for whom valid retrievals could be made. This points to the usefulness of radar for detecting weak drizzle echoes, especially below -30 dBz, and the inability of the lidar to distinguish returns due to aerosol from returns due to weak drizzle. Upon closer inspection of these variables within individual drizzle shafts, it was found that most of the low reflectivity samples correspond to either edges of evaporating drizzle shafts (e.g., hour 8:00 UTC in Figure 2a) or virga near the cloud base (e.g., hour 12:00 UTC in Figure 2a). Probing this further is outside the scope of this article, and this issue is discussed further in the last section.

3.2. Boundary Layer Properties

The average positive/negative standard deviation cloud base height and cloud top height for the entire data set were 984 ± 231 m and $1,306 \pm 265$ m, respectively. For cloud thickness and LWP the average positive/negative standard deviation was 321 ± 115 m and 101.58 ± 77 g/m², respectively. Out of 216 hr, 173 had precipitation at the cloud base, with average LWP of 115 ± 73 g/m² and cloud thickness of 344 ± 104 m. The increased cloud thickness and LWP during precipitating conditions are consistent with past observational studies (e.g., Stevens, Lenschow, Faloona, et al., 2003; Stevens, Lenschow, Vali, et al., 2003).

During the 10 cases, 22 radiosondes were launched and they all exhibited a boundary layer inversion in potential temperature and water vapor mixing ratio (Figures 4a and 4d). The average wind speed in the boundary layer was ~ 6 m/s (Figure 4c), and on average, the relative humidity showed a linear increase from $\sim 65\%$ at the surface to 100% at the cloud base. The radiative cooling at the cloud top was on average -4 K/hr (Figure 4f). None of the radiosondes showed a decoupled boundary layer or had radiative heating at the cloud top due to shortwave absorption. In spite of the fact that the cases were selected from different seasons, the variability in temperature and winds was surprisingly low. The average thermodynamic structure was similar to the classical thermodynamic and radiative structure of closed cellular marine stratocumulus clouds reported from previous field campaigns (e.g., Albrecht et al., 1995;

Comstock et al., 2007; Malinowski et al., 2013; Stevens, Lenschow, Faloona, et al., 2003; Stevens, Lenschow, Vali, et al., 2003).

The relationship between LWP, cloud thickness, cloud base RRs (R_{cb}), and radiation is further explored using the 216 hourly averages of these quantities (Figure 5). Forty-three hours (20%) had no precipitation at the cloud base, 103 hr (48%) had precipitation at the cloud base lower than 0.1 mm/day, and 70 hr (32%) had cloud base RR greater than 0.5 mm/day. The LWP increased with cloud thickness and radiative cooling at the cloud top. The relationship between LWP and R_{cb} was less defined, with presence of rain at the cloud base for the entire range of LWP and high RRs even during low LWP conditions. However, all of the hours with LWP greater than 150 g/m² were precipitating. The poor correlation between LWP and R_{cb} could be also due to mesoscale circulations carrying the in-cloud drizzle drops to thinner parts of the cloud layer. The LWP exhibited a general increase with increase in the radiative cooling at the cloud top (not shown) with significant scatter. Although a higher number of precipitating samples occurred at greater radiative cooling, the strength of precipitation itself did not show any strong relation with cloud top radiative cooling (green points in Figure 5c). This suggests that turbulence, forced by radiative cooling at the cloud top and leading to increased LWP, might be one of the factors responsible for producing drizzle, but in itself might not be sufficient for causing it. Figure 5d shows a comparison between the retrieved LWP and the LWP calculated with the adiabatic assumption (Albrecht et al. 1990). Most of the clouds were near adiabatic with the adiabaticity decreasing with increasing LWP and RRs. Thicker clouds with higher RRs have stronger turbulence and hence entrainment (Albrecht et al., 2016), which can lead to decrease in the cloud water

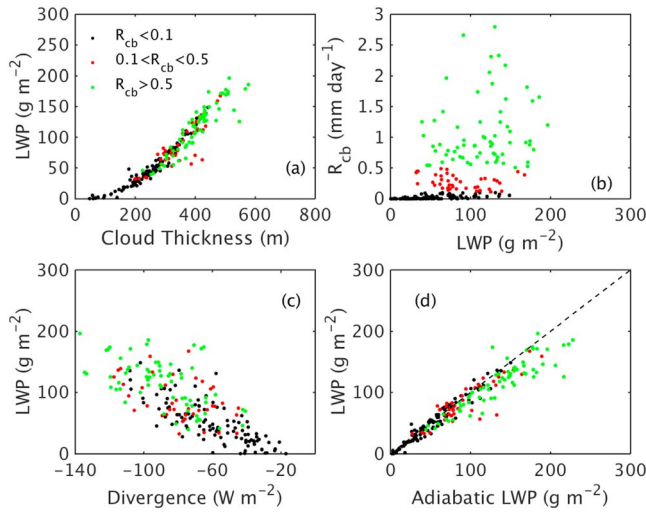


Figure 5. Scatter plots between (a) liquid water path (LWP) and cloud thickness, (b) rain rate at the cloud base (R_{cb}) and LWP, (c) LWP and radiative flux divergence near the cloud top, and (d) LWP and adiabatic LWP. There were 103 samples with $R_{cb} < 0.1$ mm/day (black), 40 samples with $0.1 < R_{cb} < 0.5$ mm/day, and 70 samples with $R_{cb} > 0.5$ mm/day.

making them subadiabatic. As the drizzle water leaving the cloud is far less than the cloud water path, these results point to entrainment, rather than precipitation, as the cause of subadiabatic LWP.

4. Drizzle Shaft Properties

In this section, the properties of drizzle shafts are examined. Drizzle shafts are defined as regions of precipitation ($R_{cb} > 0.1$ mm/day) that lasted at least 10 min. Drizzle shafts separated by less than 5 min were considered part of the same shaft, while shafts separated by more than 5 min were treated as two separate shafts. Ninety-one drizzle shafts were identified during the 10 days. Because it is not possible to probe whether the shafts went directly above the site, we only document here the average microphysical properties of drizzle shafts that lasted at least 30 min over the site, were less than 60 km wide (based on the average wind speed), and had valid drizzle retrievals for at least 75% of the time. This ensures that a sufficient number of samples are used for generating the averages reported in Table 1. This additional screening reduced the number of usable shafts to 38. Drizzle shafts identified on 4 March 2016 are shown in Figure 2a as vertical red and cyan bars. On average the width of the shafts was 28.14 km, and the shafts lasted over the site for ~85 min, with the narrowest lasting for 36 min and widest lasting for 214 min.

The widths of the drizzle shafts ranged between 11.50 and 58.45 km. The depth of drizzle (virga) shafts have been reported to be between 100 and 500 m (Yang et al., 2018). Most of the drizzle shafts had the lowest KAZR echo at 200 m above the surface; for the shafts reported here, the cloud base height is a good proxy for the virga depth. The average total LWP in the shafts was 119.22 g/m², and the average drizzle LWP below cloud base was 5.31 g/m². Although, on average, the drizzle LWP was ~5% of the total LWP, its variability was much higher with the lowest value of ~0.39 g/m² and highest value of ~17.56 g/m². This suggests that the amount of water leaving the cloud through precipitation is fairly small compared to the cloud water, but it has high variability. The drizzle modal diameter at the cloud base exhibited little variability with an average value of 138.62 microns. The RR at the cloud base (R_{cb}) was 0.98 mm/day and was near 0 at the surface consistent with complete evaporation of drizzle above the surface. Values of R_{cb} have been used to classify drizzle rates (Wood, 2012) as light ($R_{cb} < 0.5$ mm/day), moderate ($0.5 < R_{cb} < 2$ mm/day), and heavy ($R_{cb} > 2$ mm/day). Hence, most of the RRs at the cloud base for the cases analyzed here can be classified as light to moderate. The average cooling in the subcloud layer due to evaporation of

Table 1
Cloud Macrophysical Properties and Drizzle Microphysical Properties of the Selected Cases

Date	Number of drizzle shafts	Number of drizzle shafts longer than 30 min	Width of the drizzle shafts ^a (km)	Total LWP ^a (g/m ²)	Below Cloud DWP ^a (g/m ²)	Cloud base drizzle, D_m^a (μm)	Cloud base rain rate ^a (mm/day)	Surface rain rate ^b (mm/day)	Subcloud evaporation flux ^a (W/m ²)
20151019	7	1	28.15	153.43	3.35	135.50	0.62	0	-17.96
20160227	9	4	31.64	93.20	4.67	129.84	1.42	0	-41.44
20160303	6	1	23.86	112.91	0.59	137.12	0.16	0	-4.78
20160304	8	3	22.19	163.92	1.12	146.05	0.36	0	-10.36
20160409	14	8	21.86	108.79	4.10	138.57	0.79	0.01	-22.95
20160628	5	3	21.65	99.14	4.81	162.33	0.95	0.01	-27.44
20161015	4	2	32.15	168.90	13.45	152.15	1.41	0	-41.00
20161031	18	7	36.47	134.82	5.62	133.44	0.90	0.01	-26.09
20161116	8	3	42.47	126.69	3.72	144.83	0.99	0.03	-28.57
20161117	12	6	22.88	95.04	8.54	136.99	1.31	0.21	-37.94
All	91	38	28.14 ± 12.42	119.22 ± 34.33	5.31 ± 4.49	138.62 ± 14.02	0.98 ± 0.72	0.04 ± 0.21	-28.68 ± 29.11

^aOnly calculated for drizzle shafts that lasted longer than 30 min over the radar. ^bDue to very low values, zeros were treated as NaNs while taking averages.

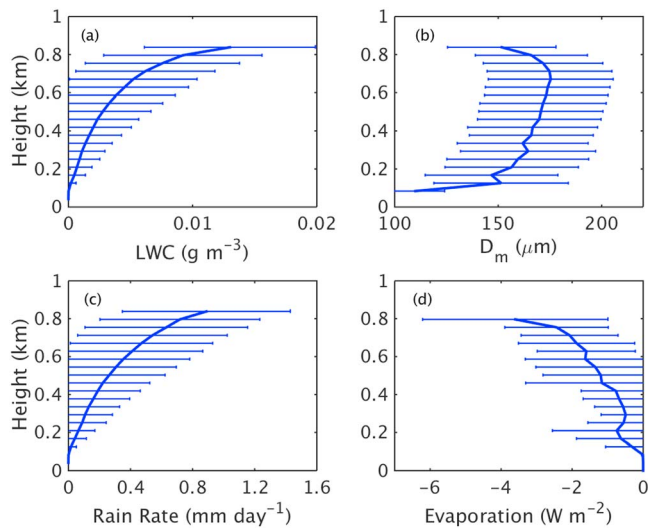


Figure 6. Average profile of drizzle liquid water content (LWC; a), D_m (b), rain rate (c), and evaporation flux (d) calculated for the 38 drizzle shafts lasting for more than 30 min over the radar. The horizontal bars show the one standard deviation from the mean.

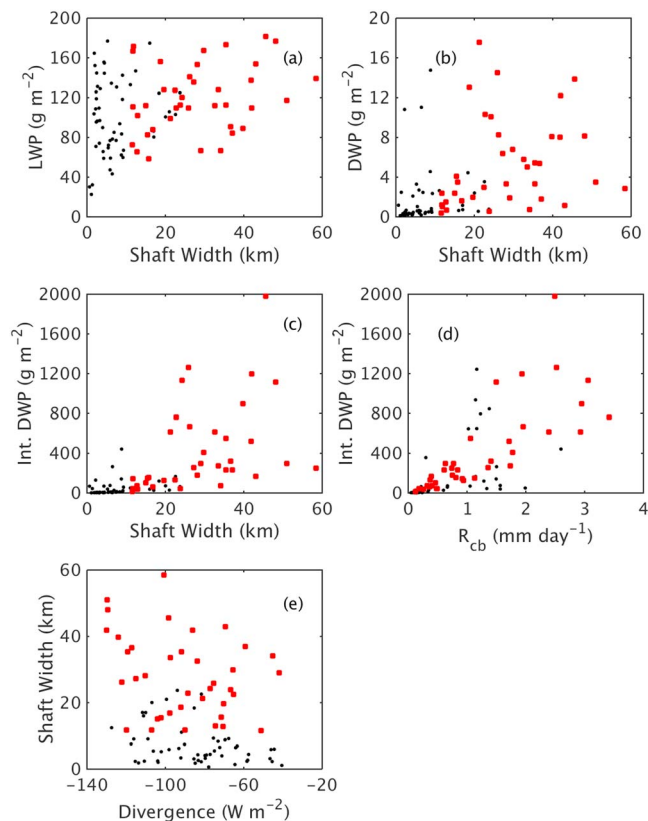


Figure 7. Scatter plots between (a) shaft width and liquid water path (LWP), (b) shaft width and drizzle water path (DWP), (c) shaft width and integrated drizzle water path, (d) rain rate and integrated drizzle water path, and (e) radiative flux divergence at the cloud top and shaft width. Black symbols indicate all shafts and red symbols indicate shafts that lasted at least 30 min over the site.

drizzle drops was -28.68 W/m^2 , with the highest observed cooling of -87.08 W/m^2 and lowest of -3.16 W/m^2 . These cooling rates are at times comparable to the radiative cooling near the cloud top (discussed later). Unlike the cloud top radiative cooling that is confined to a very small layer, the evaporative cooling in the subcloud layer is distributed within a 1-km layer (cloud base height). For an average cooling of -28.68 W/m^2 distributed over a layer of 989 m, the diabatic cooling rate would be -2.08 K/day , which is substantial and almost half of the average radiative cooling rate at the cloud top.

To gain insight into the profiles of microphysical properties within the drizzle shafts, the derived microphysical properties were averaged within the shafts (Figure 6). For producing the averages, the RRs and LWCs of hydrometeor-free regions were set to 0, and the modal diameters of those regions were treated as missing. The shaft-averaged profiles of LWC and RR decreased from cloud base to almost zero value near the surface. Due to differences in the drizzle shaft depths, the standard deviation of LWC and RR was substantial and comparable to the mean, especially in the lower half of the subcloud layer. The modal diameter increased right below the cloud base, denoting evaporation of smaller drizzle drops, and then exhibited a general decrease below that. The values of modal diameter were similar within most of the shafts with an average value of $166.64 \mu\text{m}$ and standard deviation of $31.35 \mu\text{m}$ in the middle of the subcloud layer. The profile of evaporative flux was calculated from the profile of RRs and had an average value of -3.5 W/m^2 right below the cloud base and 0 near the surface, with an average total cooling of -30.60 W/m^2 . The standard deviation of the evaporative flux was largest immediately below the cloud base where the biggest change in RR occurred, evaporating most of small drizzle drops. Apart from minimal variations in the lower half of the subcloud layer, the evaporation flux decreased almost linearly from its value below the cloud base. The profiles of individual shafts (not shown) confirmed that most of the drizzle evaporation happens within 200 m of the cloud base.

We further focus on the relationship between the width of the drizzle shafts and other precipitation and boundary layer variables. Due to the high amount of scatter, none of the scatter plots revealed statistically significant relationships; however, collectively, the plots shed some insights on boundary layer microphysical processes. The radiative flux divergence at the cloud top did not show any systematic relationship with shaft-averaged RRs nor with the modal diameter. However, drizzle shafts with RRs greater 2 mm/day had radiative flux divergence lower than -60 W/m^2 , suggesting that cloud top cooling plays some role in drizzle production. Similarly, the modal diameter did not show any systematic relationship with the width of drizzle shafts. On average the LWP and DWP exhibited a weak positive correlation with the shaft width (Figures 7a and 7b), and the shaft width exhibited a weak positive correlation with the radiative cooling at the cloud top (Figure 7e). This suggests that a stronger radiative cooling leads to thicker clouds (increased LWP) with wider precipitating cells, which results in higher amount of liquid water being removed from the cloud. The increase in the drizzle shaft width associated with higher radiative cooling is loosely consistent with the higher nighttime cell aspect ratio and LWP reported by Kazil et al. (2017) for closed cellular stratocumuli. However, our results are not statistically significant to confirm this hypothesis.

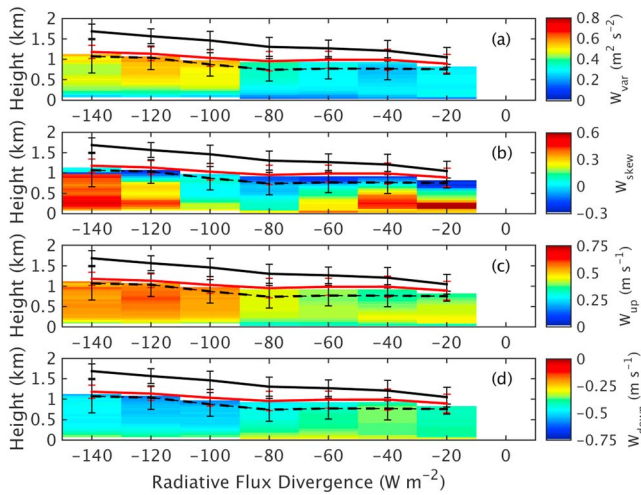


Figure 8. Profiles of (a) variance of vertical velocity, (b) skewness of vertical velocity, (c) updraft strength, and (d) downdraft strength binned by radiative flux divergence at the cloud top. The cloud top height (solid black), cloud base height (solid red), and lifting condensation level (dashed black) are shown in each panel. The vertical lines show the one standard deviation from the mean. The number of samples in each bin are 4, 17, 36, 62, 56, 37, and 4 for six divergence bins from -140 to 0 W m^{-2} with a width of 20 W m^{-2} .

these cloud systems (Figure 8). The cloud base and top height along with the cloud thickness increased with increasing radiative flux divergence. The difference between the LCL and the cloud base height was higher for radiative cooling values between -40 and -80 W m^{-2} indicating boundary layer decoupling. As expected, the variance of vertical velocity increased with increasing cloud top radiative cooling from ~ 0.2 m^2/s^2 at -20

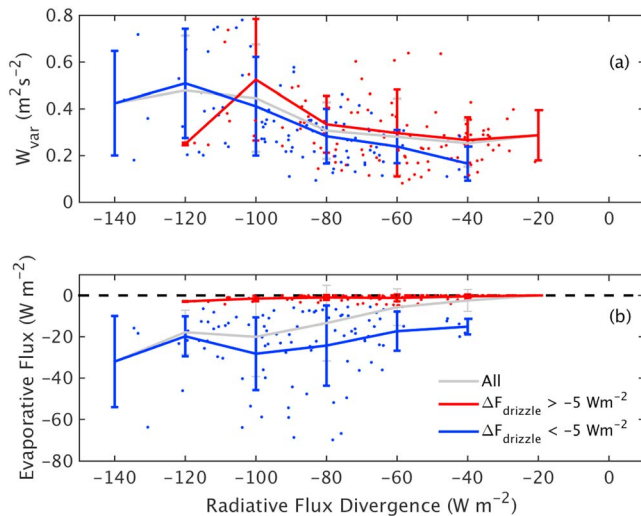


Figure 9. (a) Average below-cloud variance of vertical velocity binned by the radiative flux divergence near the cloud top. (b) Average drizzle evaporative cooling below cloud base ($\Delta F_{\text{drizzle}}$) binned by the radiative flux divergence near the cloud top. Gray lines represent the average of all samples; red and blue lines represent the average of samples with $\Delta F_{\text{drizzle}} > -5$ W m^{-2} and $\Delta F_{\text{drizzle}} < -5$ W m^{-2} , respectively. Vertical lines represent the standard deviation in each bin. Available samples in each bin from -140 to 0 W m^{-2} are 4, 17, 36, 62, 54, 37, and 4 for the black line; 0, 2, 11, 29, 39, 32, and 4 for the red line; and 4, 15, 25, 33, 15, 5, and 0 for the blue line. The bin size is 20 W m^{-2} .

To understand whether wider shafts or stronger RRs are more efficient in removing water from the cloud layer, the shaft-integrated DWP, that is, the sum of DWP within the shaft period, was calculated. The shaft-integrated DWP represents the total amount of water removed from the cloud by a drizzle shaft. The shaft-integrated DWP varied between 12.35 and $\sim 2,000$ g m^{-2} for moderately precipitating drizzle shafts. The average ratio of DWP to LWP was 0.045, which suggests that the liquid water below cloud base is only $\sim 5\%$ of the total water within the boundary layer. The depletion timescale (Wood, 2005), which is the ratio of total LWP to the RR at the cloud base, was on average about 4 hr. Although with substantial scatter, the shaft-integrated DWP increased with the shaft width and with shaft-averaged R_{cb} (Figures 7c and 7d). This suggests that the rain fraction and RRs are equally important in determining the amount of condensate removed from the cloud. The depletion timescales did not reveal any systematic relationship with LWP, DWP, or shaft-integrated DWP.

5. Turbulence Properties

In this section, the turbulence properties of the subcloud layers of drizzling clouds are examined. Hourly profiles of statistical parameters of vertical velocity and cloud boundaries were binned by the radiative flux divergence at the cloud top, which is the primary forcing mechanism for these cloud systems (Figure 8). The cloud base and top height along with the cloud thickness increased with increasing radiative flux divergence. The difference between the LCL and the cloud base height was higher for radiative cooling values between -40 and -80 W m^{-2} indicating boundary layer decoupling. As expected, the variance of vertical velocity increased with increasing cloud top radiative cooling from ~ 0.2 m^2/s^2 at -20 W m^{-2} to ~ 0.5 m^2/s^2 at -140 W m^{-2} (Figure 8a). The high variance below 500 m, which is present for weak cloud top radiative cooling (-40 and -20 W m^{-2}) could be due to increased cumuliform convection below stratiform clouds for these conditions. On average the skewness of vertical velocity was always positive and was higher in the lower half of the subcloud layer than in the upper half. This is consistent with previous observations (Ghate et al., 2014; Stevens, Lenschow, Faloona, et al., 2003; Stevens, Lenschow, Vali, et al., 2003) and Large Eddy Simulation (LES) model simulations (Ackerman et al., 2009) of positive skewness in the subcloud layer and negative skewness in the cloud layer. The updraft and downdraft strengths (Figures 8c and d) increased with increasing cloud top radiative cooling as well, reaching magnitudes over 0.7 m/s for strong radiative cooling. It is important to note that the shown profiles only refer to below-cloud conditions and the turbulence profiles in the cloud layer could be vastly different (i.e., negative skewness) than those shown in Figure 8.

To assess the impact of drizzle evaporation-induced cooling on boundary layer turbulence, the vertically averaged variance of vertical velocity below cloud base (W_{var}) and the total evaporative cooling in the subcloud layer ($\Delta F_{\text{drizzle}}$) binned by the radiative flux divergence at the cloud top are shown in Figure 9. Although with substantial scatter, both W_{var} and $\Delta F_{\text{drizzle}}$ increased in magnitude with cloud top radiative flux divergence (gray lines in Figure 9). Cases with weak radiative cooling (-20 W m^{-2}) had no precipitation, conversely all cases with cooling stronger than -120 W m^{-2} were precipitating. These results are consistent with a scenario of higher RRs at night accompanied by strong radiative cooling

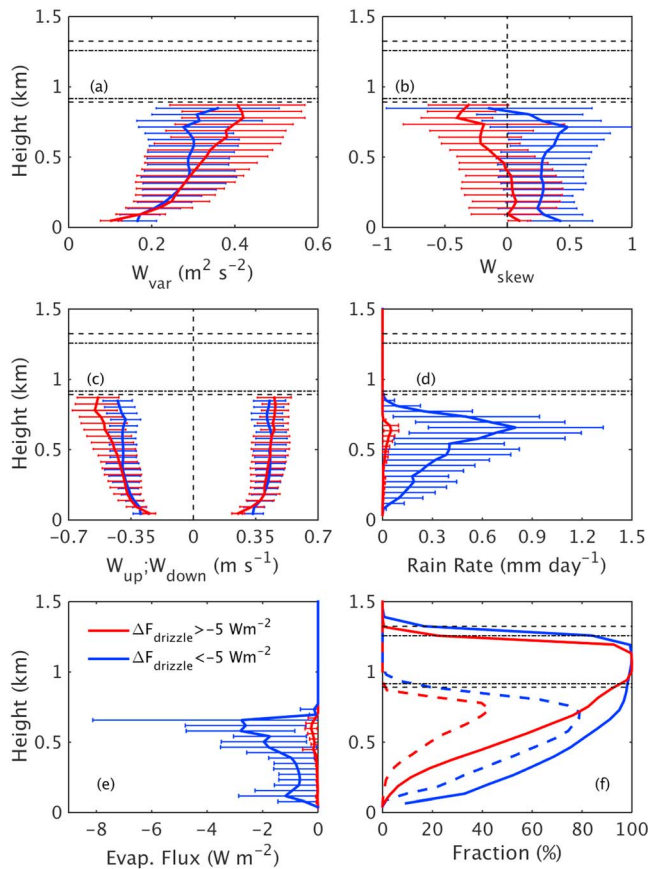


Figure 10. Average profiles of (a) variance of vertical velocity, (b) skewness of vertical velocity, (c) updraft and downdraft strength, (d) rain rate, (e) evaporative flux, and (f) Ka-band ARM Zenith Radar echo fraction (solid) and retrieval fraction (dashed) during hours with $\Delta F_{\text{drizzle}} > -5 \text{ W/m}^2$ (red) and $\Delta F_{\text{drizzle}} < -5 \text{ W/m}^2$ (blue). The horizontal bars in panels a–e denote one standard deviation from the mean. Average cloud boundaries for $\Delta F_{\text{drizzle}} > -5 \text{ W/m}^2$ (dash-dot) and $\Delta F_{\text{drizzle}} < -5 \text{ W/m}^2$ (dash) are shown in all panels except (e). Twenty-one samples each were available for the classification.

and nonprecipitating conditions during the day associated with weaker radiative cooling.

The scatter in Figure 9b shows several instances during which the radiative cooling at the cloud top is of the same magnitude as the drizzle evaporative cooling. To eliminate weakly precipitating drizzle cells and to remove edges of drizzle shafts within the hourly samples, the cases were further classified based on a threshold of $\Delta F_{\text{drizzle}} = -5 \text{ W/m}^2$. We refer to the subset with total $\Delta F_{\text{drizzle}} > -5 \text{ W/m}^2$ (shown in red) as weakly drizzling and with $\Delta F_{\text{drizzle}} < -5 \text{ W/m}^2$ (shown in blue) as strongly drizzling. In this manner, 97 hr were identified as strongly drizzling and 126 hr as weakly drizzling. It can be seen that W_{var} is always higher for the weakly drizzling subset as compared to the strongly drizzling, with the only exception of the last bin (-120 W/m^2) that had only four weakly drizzling samples. The average variance of vertical velocity during weakly drizzling hours was $0.31 \pm 0.16 \text{ m}^2/\text{s}^2$, while the same during strongly drizzling hours was $0.34 \pm 0.19 \text{ m}^2/\text{s}^2$. The slightly higher variance of vertical velocity during strongly drizzling hours is due to the higher number of strongly drizzling samples during strong radiative cooling and weakly drizzling samples during weak radiative cooling. The average variance of vertical velocity of the 71 strongly drizzling samples that had radiative cooling between -110 and -60 W/m^2 was $0.32 + 0.17 \text{ m}^2/\text{s}^2$, while the same for the 58 weakly drizzling samples was $0.38 + 0.20 \text{ m}^2/\text{s}^2$. The results suggest that, for similar amount of radiative cooling at the cloud top, the cooling due to evaporation of drizzle drops reduces the variance of vertical velocity by $\sim 16\%$. We emphasize here that the values shown in Figure 9 are averaged over the subcloud vertical layers and differences in the profiles of variance between the two subsets are probably greater near the cloud base, where most of the evaporation is concentrated.

The vertical profiles of turbulence and drizzle properties are further explored for samples with radiative cooling ΔF_{rad} between -110 and -60 W/m^2 and cloud base height lower than 1,200 m and are shown in Figure 10. Twenty-one samples each were available for weakly drizzling shafts ($-110 > \Delta F_{\text{rad}} > -60$ and $\Delta F_{\text{drizzle}} > -5 \text{ W/m}^2$) and for strongly drizzling shafts ($-110 > \Delta F_{\text{rad}} > -60$ and $\Delta F_{\text{drizzle}} < -5 \text{ W/m}^2$). The

average positive/negative standard deviation radiative flux divergence at the cloud top was $-81.71 \pm 14.11 \text{ W/m}^2$ and $-75.12 \pm 11.91 \text{ W/m}^2$ for strongly drizzling and weakly drizzling samples, respectively, with LWP of $183.62 \pm 64.63 \text{ g/m}^2$ and $107.11 \pm 47.96 \text{ g/m}^2$. The cloud base heights were similar for the subsets, conversely the strongly drizzling subset had higher cloud top heights. Figure 10a shows that the variance of vertical velocity was on average significantly lower for the strongly drizzling subset owing to the contribution of the layers immediately below the cloud base. For example, $\sim 100 \text{ m}$ below the cloud base, the difference between the two subsets was on average $0.1 \text{ m}^2/\text{s}^2$ ($\sim 27\%$). The average skewness of vertical velocity was positive for strongly drizzling cases and negative for weakly drizzling cases (Figure 10b). Differences in the skewness in the upper half of the subcloud layer were primarily due to reduction in the strengths of downdrafts as the average profiles of updraft strength (Figure 10c) were similar for the subsets. On average, the downdrafts during the strongly drizzling hours were weaker as compared to those during weakly drizzling hours. The averaged profiles of RRs and evaporative flux shown in Figures 10d and 10e indicate that most of the evaporation occurred within 100 m of the cloud base. Finally, Figure 10f shows the profiles of KAZR echo fraction (solid) and retrieval fraction (dashed) for the two subsets. Figure 10f shows that the KAZR signal was present almost 100% of the times in both subsets; however, retrievals for the weakly drizzling cases were present only in limited amount due to the fact that for the ceilometer the drizzle echo is not significantly higher than the aerosol echo (hence no retrievals). Collectively, Figure 10 demonstrates that for

similar conditions of radiative cooling near the cloud top, evaporation of drizzle drops in the subcloud layer has an impact on the boundary layer turbulence, affecting primarily the layer immediately below the cloud base.

6. Summary, Discussion, and Conclusion

Drizzle is ubiquitous in marine stratocumulus clouds, and it largely evaporates in the subsaturated subcloud layer. We have used data collected at the ARM ENA site during 10 days of closed cellular (completely overcast) conditions to report the average drizzle properties and assess the impact of drizzle evaporation-induced cooling on the boundary layer turbulence. The retrieval technique that combines data from lidar ceilometer and cloud radar was used to retrieve profiles of drizzle microphysical properties below the cloud base. The retrieval technique in the current setup was ineffective to retrieve the edges of the drizzle shafts and weak drizzle. A retrieval technique that uses data from a combination radars and lidars at different frequencies might be able to retrieve drizzle properties of the weak virga.

The retrieved drizzle microphysical properties were used in conjunction with a microwave scattering radiative transfer model to retrieve IWV and LWP accounting for the scattering properties of hydrometeors. The retrievals were used to investigate general features of the turbulent boundary layer, the properties of drizzle shafts, and the effect of drizzle on boundary layer turbulence. The main findings are summarized below:

1. In the 216 hr of data analyzed in this study, 91 drizzle shafts were identified. Out of the 91 shafts 38 lasted more than 30 min over the site. On average the drizzle shafts were 28.14 km wide with an average RR and modal diameter at the cloud base of 0.98 mm/day and $-138.62 \mu\text{m}$, respectively. The RR at the surface was almost negligible yielding an average diabatic cooling of -28.68 W/m^2 in the subcloud layer.
2. LWP increased with the radiative cooling at the cloud top but did not show a clear relation with cloud base RR (R_{cb}). However, the number of precipitating samples increased with an increase in the radiative cooling. This suggests that greater LWP and radiative cooling provide necessary conditions for producing drizzle; however, the magnitude of the RRs is determined by other processes.
3. The total water removed from the cloud within a drizzle shaft ranged between 12.25 and over 2,000 g/m^2 and was several times greater than the total LWP suggesting replenishing of condensate within the drizzle shafts. The total water removed by drizzle within the shafts presented a relation with both the width of drizzle shafts and the RR at cloud base. This suggests that both parameters (rain area and strength) are important in determining the amount of condensate leaving the cloud.
4. When binned by the radiative flux divergence near the cloud top, the turbulence profiles below cloud base agreed with the classical view of stratocumulus clouds having higher turbulence for higher radiative cooling. For a similar amount of radiative cooling at the cloud top, the average variance of vertical velocity in the subcloud layer was about 16% lower during strongly precipitating hours than during weakly precipitating hours. This reduction in variance of vertical velocity was due to reduction in the strengths of the downdrafts in the upper half of the subcloud layer. Previous studies of closed cellular stratocumulus cloud systems have reported cell sizes of 20–60 km (Wood & Hartmann, 2006), widths of the drizzle shafts between 2 and 20 km (Wood, 2005), and changes in the cell sizes on diurnal timescales (Kazil et al., 2017). In this study, the widths of the drizzle shafts exhibited a modest increase with increasing radiative cooling near the cloud top. Although this result was not statistically significant, it points toward changes in rain area fraction with boundary layer forcing. One of the reasons of the lack of statistically significant correlation could be the inherently flawed comparison of a mesoscale quantity such as shaft width with submesoscale quantities such as LWP, DWP, and RR_{CB} . A plot similar to Figure 7 made from the top 10% LWP, DWP, and RR_{CB} within the shafts also did not yield any significant correlation. A more comprehensive approach that characterizes these quantities at the same spatial scales might shed useful insights on the impact of mesoscale variables on cloud-scale variables. Collocated observations from scanning precipitation radars and scanning MWRs could provide such an information. The upper half of the subcloud layer was found to have lower turbulence during strongly precipitating conditions than during weakly precipitating conditions for a similar amount of radiative cooling. Although yielding insights on the depth of the layer affected by drizzle evaporation, it is possible for this layer to be different than the thermodynamic layer impacted by drizzle evaporation. Observations from a collocated Raman lidar, which were not available for the cases analyzed here, might shed some light on the impact of drizzle

evaporation on boundary layer thermodynamics and perhaps cold pools (Wilbanks et al., 2015) associated with these systems. These could be used to assess whether drizzle evaporation can lead to thermodynamic decoupling. Stratocumulus topped boundary layers (STBLs) with stronger radiative cooling at the cloud top are often deeper, have higher turbulence, and hence have higher collision-coalescence rates leading to drizzle formation than those with weaker radiative cooling. Thus, the cloud base RRs and cooling due to drizzle evaporation are higher in strongly forced (and turbulent) STBLs than in weakly forced STBLs. Although the strongly forced and more turbulent STBLs have higher evaporative cooling, the impact of evaporative cooling on turbulence might be greater in weakly forced STBLs. Hence, drizzle evaporative cooling could be potentially represented as a function of cloud top radiative cooling, however, not its impact on boundary layer turbulence. It is puzzling that the magnitude of downdrafts was lower during strongly precipitating conditions than during weakly precipitating conditions with the magnitude of updrafts largely unchanged. If the drizzle drops evaporate in the downdrafts then the evaporative cooling will further increase their strength. However, if the drizzle drops evaporate in the updraft, it will reduce their strength and subsequently, by continuity, decrease the strength of following downdrafts. In this study, we have focused on drizzle evaporation on the scales of the drizzle shafts (approximately tens of kilometers), a closer inspection of drizzle evaporation and vertical air motion at finer timescales might shed some more insights on which one of the two mechanisms is more prevalent. Lastly, in this study, the drizzle retrievals were only produced below the cloud base, with the ratio of below cloud base DWP to total water path being about 5%. The combination of radar Doppler spectra and the optimal estimation techniques could be further used to characterize drizzle properties above the cloud base and examine the amount of drizzle water leaving the cloud. The turbulence within these systems might prevent the drizzle drops from escaping the cloud, until they have reached certain sizes. Probing this further will also help to disentangle the complex aerosol-cloud-precipitation interactions associated with the marine stratocumulus cloud systems.

Appendix A: Ceilometer Calibration

The first step in the calibration process was to calculate the backscatter and volume extinction coefficients for spherical water drops at 905-nm wavelength and 8.6-mm wavelength using the Mie theory (Wiscombe, 1988). The refractive index of water at 905 nm was set to $1.328 + i6.72 \times 10^{-7}$ and at 8.6 mm

was set to $5.22 + i2.80$. The calculated backscatter and extinction coefficients for single drops were integrated to calculate the lidar ratio and Mie-to-Rayleigh ratio for a Gamma DSDs of different modal diameter and shape parameters at 905-nm and 8.66-mm wavelengths, respectively.

The calculated average lidar ratio at 905-nm wavelength for a Gamma DSD with modal diameter between 10 and 50 μm was found to be 18.87 Sr with a standard deviation of 0.78 Sr. Data collected during 7 March 2016 were used to calibrate the ceilometer (Figure A1). Nonprecipitating stratocumulus clouds were observed during the first 6 hr. Between 6:00 and 10:00 UTC, light precipitation was observed, thereby increasing the integrated backscatter and decreasing the lidar ratio. Because the raw uncalibrated lidar ratio during nonprecipitating conditions was 23.74 Sr, we applied a calibration constant $C = 1.2744$ to match the lidar ratio to the theoretical value of 18.87 Sr.

Appendix B: LWP Retrievals From KAZR-Ceilometer-MWR3C

The retrieval of precipitable water vapor and LWP from combined active and passive sensor is based on the optimal estimation technique described in Cadetdu et al. (2017). The retrieval uses the Passive and Active Microwave TRANSfer model to simulate brightness temperatures under the assumption of scattering or nonscattering conditions, provided the knowledge of hydrometeor DSD. In the present work, the average drop size of the hydrometeors and the vertical profiles of drizzle LWC below

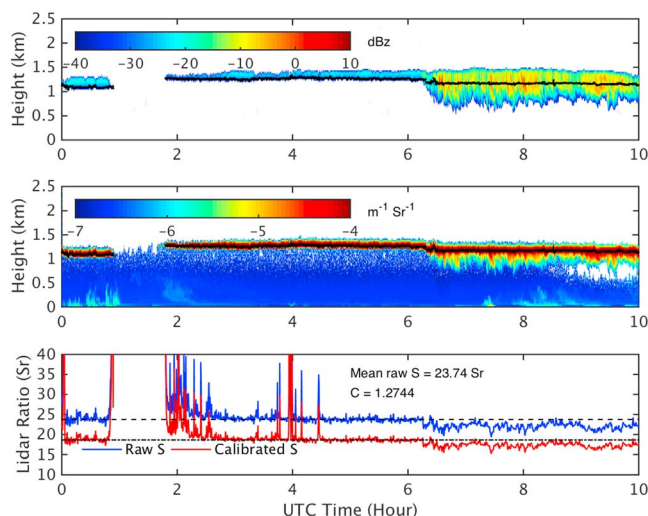


Figure A1. (top) Time-height profiles of Ka-band ARM Zenith Radar reflectivity (shades) and ceilometer cloud base height (black). (middle) Time-height profiles of ceilometer backscatter (shades) and ceilometer cloud base height (black). (bottom) Time series of uncalibrated (blue) and calibrated (red) lidar ratio S . The dashed line and dot-dash line corresponds to the mean uncalibrated and the reference lidar ratio of 18.87 Sr, respectively. The data were collected on 7 March 2016 at the Eastern North Atlantic site.

Retrieval development part II: Active and passive

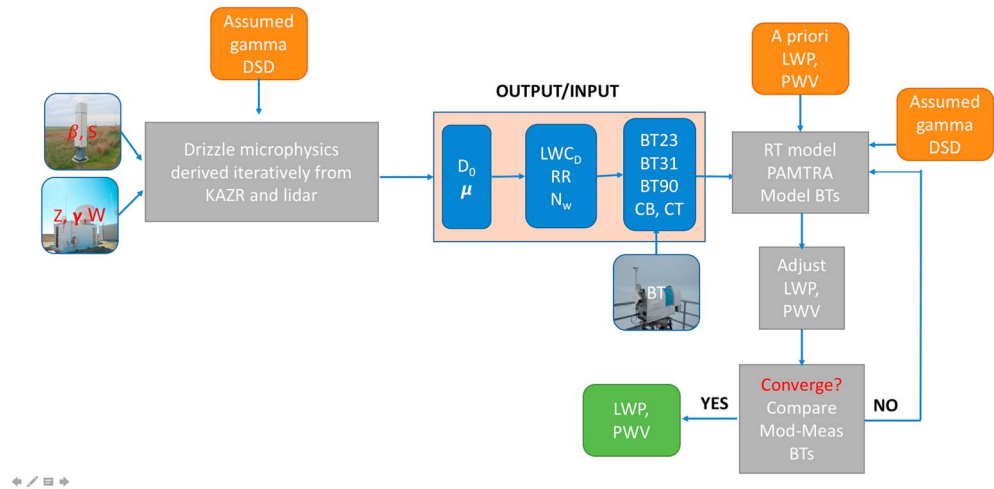


Figure A2. Flow chart describing the LWP retrieval by combining data from KAZR, ceilometer, and MWR3C. LWliquid water path; RR = rain rate; LWC = liquid water content; PWV = precipitable water vapor; FAMTRA = Passive and Active Microwave TRANSfer model; KAZR = Ka-band Atmospheric Radiation Measurement Zenith Radar; DSD = drop size distribution.

cloud base derived from the active (KAZR + Ceilometer) retrieval were provided to the radiative transfer model and constrained during the retrieval process. Additional information provided includes the cloud base and cloud top derived from the ceilometer and the KAZR. For the radiative transfer model, information on the DSD and LWC between cloud base and cloud top is necessary. As this information was not available due to lack of retrievals above the cloud base, some assumptions had to be made.

The total LWC between cloud base and top was partitioned between cloud and drizzle. The drizzle LWC in the cloud was assumed constant with value equal to the LWC at cloud base. The total integrated drizzle LWP (above and below cloud base) was then subtracted from the first guess total LWP provided by the NN algorithm to provide a first guess cloud LWP. This latest was then distributed adiabatically between cloud base and top. The effective radius of the in-cloud DSD was assumed to be $20 \mu\text{m}$ if the cloud was not precipitating. If the cloud was precipitating, an estimate of the effective radius at the cloud base was computed when the radar signal was present and was assumed to be valid for the whole cloud. A flowchart of the active/passive retrieval is shown in Figure A2. The output of the retrieval is the total LWP, precipitable water vapor, and C_F , the fraction of cloud to total LWP.

References

- Ackerman, A. S., vanZanten, M. C., Stevens, B., Savic-Jovicic, V., Bretherton, C. S., Chlond, A., et al. (2009). Large-eddy simulations of a drizzling, stratocumulus-topped marine boundary layer. *Monthly Weather Review*, *137*(3), 1083–1110. <https://doi.org/10.1175/2008MWR2582.1>
- Ahlgrim, M., & Forbes, R. (2014). Improving the representation of low clouds and drizzle in the ECMWF model based on ARM observations from the Azores. *Monthly Weather Review*, *142*(2), 668–685. <https://doi.org/10.1175/MWR-D-13-00153.1>
- Albrecht, B., Fang, M., & Ghate, V. (2016). Exploring stratocumulus cloud-top entrainment processes and parameterizations by using Doppler cloud radar observations. *Journal of the Atmospheric Sciences*, *73*(2), 729–742. <https://doi.org/10.1175/JAS-D-15-0147.1>
- Albrecht, B. A., Bretherton, C. S., Johnson, D., Schubert, W. H., & Frisch, A. S. (1995). The Atlantic Stratocumulus Transition Experiment —ASTEX. *Bulletin of the American Meteorological Society*, *76*(6), 889–904. [https://doi.org/10.1175/1520-0477\(1995\)076<0889:TASTE>2.0.CO;2](https://doi.org/10.1175/1520-0477(1995)076<0889:TASTE>2.0.CO;2)
- Albrecht, B. A., Fairall, C. W., Thompson, D. W., White, A. B., Snider, J. B., & Schubert, W. H. (1990). Surface based remote sensing of the observed and adiabatic liquid water content of stratocumulus clouds. *Geophysical Research Letters*.
- Bogenschutz, P. A., Gettelman, A., Morrison, H., Larson, V. E., Craig, C., & Schanen, D. P. (2013). Higher-order turbulence closure and its impact on climate simulations in the Community Atmosphere Model. *Journal of Climate*, *26*(23), 9655–9676. <https://doi.org/10.1175/JCLI-D-13-00075.1>
- Bolton, D. (1980). The computation of equivalent potential temperature. *Monthly Weather Review*, *108*(7), 1046–1053. [https://doi.org/10.1175/1520-0493\(1980\)108<1046:TCOEPT>2.0.CO;2](https://doi.org/10.1175/1520-0493(1980)108<1046:TCOEPT>2.0.CO;2)
- Borque, P., Luke, E. P., Kollias, P., & Yang, F. (2018). Relationship between turbulence and drizzle in continental and marine low stratiform clouds. *Journal of the Atmospheric Sciences*, *75*(12), 4139–4148. <https://doi.org/10.1175/JAS-D-18-0060.1>

Acknowledgments

The authors would like to thank Robert Wood, Steve Klein, and Xue Zheng for helpful discussions. V. G. was supported by the National Science Foundation (NSF) grant AGS-1445831 awarded to the University of Chicago and the U.S. Department of Energy's (DOE) Atmospheric System Research (ASR), an Office of Science, Office of Biological and Environmental Research (BER) program, under contract DE-AC02-06CH11357 awarded to Argonne National Laboratory. M. C. is supported by the U.S. Department of Energy, Office of Science, Office of Biological and Environmental Research, Atmospheric Radiation Measurement Infrastructure, under contract DE-AC02-06CH11357. The ground-based data used in this study were obtained from the Atmospheric Radiation Measurement (ARM) user facility, a U.S. Department of Energy (DOE) Office of Science user facility managed by the Office of Biological and Environmental Research. The satellite data were obtained from the NASA Langley Research Center Atmospheric Science Data Center. We gratefully acknowledge the computing resources provided on Blues, a high-performance computing cluster operated by the Laboratory Computing Resource Center (LCRC) at the Argonne National Laboratory. The ARM data are available at archive.arm.gov, and the satellite data are available at satcorps.larc.nasa.gov.

- Cadeddu, M. P., Liljegren, J. C., & Turner, D. D. (2013). The Atmospheric radiation measurement (ARM) program network of microwave radiometers: instrumentation, data, and retrievals. *Atmospheric Measurement Techniques*, 6, 2359–2372. <https://doi.org/10.5194/amt-6-2359-2013>
- Cadeddu, M. P., Marchand, R., Orlandi, E., Turner, D. D., & Mech, M. (2017). Microwave passive ground-based retrievals of cloud and rain liquid water path in drizzling clouds: Challenges and possibilities. *IEEE Transactions on Geoscience and Remote Sensing*, 55(11), 6468–6481. <https://doi.org/10.1109/TGRS.2017.2728699>
- Clothiaux, E. E., Ackerman, T. P., Mace, G. G., Moran, K. P., Marchand, R. T., Miller, M. A., & Martner, B. E. (2000). Objective determination of cloud heights and radar reflectivities using a combination of active remote sensors at the ARM CART sites. *Journal of Applied Meteorology*, 39(5), 645–665. [https://doi.org/10.1175/1520-0450\(2000\)039<0645:ODOCHA>2.0.CO;2](https://doi.org/10.1175/1520-0450(2000)039<0645:ODOCHA>2.0.CO;2)
- Comstock, K., Yuter, S. E., Wood, R., & Bretherton, C. S. (2007). The three dimensional structure and kinematics of drizzling stratocumulus. *Monthly Weather Review*, 135(11), 3767–3784. <https://doi.org/10.1175/2007MWR1944.1>
- Feingold, G., Koren, I., Yamaguchi, T., & Kazil, J. (2015). On the reversibility of transitions between closed and open cellular convection. *Atmospheric Chemistry and Physics*, 15(13), 7351–7367. <https://doi.org/10.5194/acp-15-7351-2015>
- Frisch, A. S., Fairall, C. W., & Snider, J. B. (1995). Measurement of stratus cloud and drizzle parameters in ASTEX with a K α -band Doppler radar and a microwave radiometer. *Journal of the Atmospheric Sciences*, 52(16), 2788–2799. [https://doi.org/10.1175/1520-0469\(1995\)052<2788:MOSCAD>2.0.CO;2](https://doi.org/10.1175/1520-0469(1995)052<2788:MOSCAD>2.0.CO;2)
- Gettelman, A., & Morrison, H. (2015). Advanced two-moment bulk microphysics for global models: Part I: Off-line tests and comparison with other schemes. *Journal of Climate*, 28(3), 1268–1287. <https://doi.org/10.1175/JCLI-D-14-00102.1>
- Ghate, V. P., Albrecht, B. A., Miller, M. A., Brewer, A., & Fairall, C. W. (2014). Turbulence and radiation in a stratocumulus topped marine boundary layer: A case-study from VOCALS REX. *Journal of Applied Meteorology and Climatology*, 53(1), 117–135. <https://doi.org/10.1175/JAMC-D-12-0225.1>
- Ghate, V. P., Miller, M. A., Albrecht, B. A., & Fairall, C. W. (2015). Thermodynamic and radiative structure of stratocumulus-topped boundary layers. *Journal of the Atmospheric Sciences*, 72(1), 430–451. <https://doi.org/10.1175/JAS-D-13-0313.1>
- Ghate, V. P., Miller, M. A., & Zhu, P. (2016). Differences between nonprecipitating tropical and trade wind marine shallow cumuli. *Monthly Weather Review*, 144(2), 681–701. <https://doi.org/10.1175/MWR-D-15-0110.1>
- Golaz, J.-C., Larson, V. E., & Cotton, W. R. (2002). A PDF-based model for boundary layer clouds. Part I: Method and model description. *Journal of the Atmospheric Sciences*, 59(24), 3540–3551. [https://doi.org/10.1175/15200469\(2002\)059<3540:APBMFB>2.0.CO;2](https://doi.org/10.1175/15200469(2002)059<3540:APBMFB>2.0.CO;2)
- Gossard, E. E., Strauch, R. O., & Rogers, R. R. (1990). Evolution of droplet size distributions in liquid precipitation observed by ground-based Doppler radar. *Journal of Atmospheric and Oceanic Technology*, 7(6), 815–828. [https://doi.org/10.1175/1520-0426\(1990\)007<0815:EODDIL>2.0.CO;2](https://doi.org/10.1175/1520-0426(1990)007<0815:EODDIL>2.0.CO;2)
- Iacono, M. J., Mlawer, E. J., Clough, S. A., & Morcrette, J.-J. (2000). Impact of an improved longwave radiation model, RRTM on the energy budget and thermodynamic properties of the NCAR Community Climate Model, CCM3. *Journal of Geophysical Research*, 105(D11), 14,873–14,890. <https://doi.org/10.1029/2000JD900091>
- Kazil, J., Yamaguchi, T., & Feingold, G. (2017). Mesoscale organization, entrainment, and the properties of a closed-cell stratocumulus cloud. *Journal of Advances in Modeling Earth Systems*, 9, 2214–2229. <https://doi.org/10.1002/2017MS001072>
- Klein, S. A., & Hartmann, D. L. (1993). The seasonal cycle of low stratiform clouds. *Journal of Climate*, 6(8), 1587–1606. [https://doi.org/10.1175/1520-0442\(1993\)006<1587:TSCOLS>2.0.CO;2](https://doi.org/10.1175/1520-0442(1993)006<1587:TSCOLS>2.0.CO;2)
- Kottahaus, S., O'Connor, E., Munkel, C., Charlton-Perez, C., Haefelin, M., Gabey, A. M., & Grimmond, C. S. B. (2016). Recommendations for processing atmospheric attenuated backscatter profiles from Vaisala CL31 ceilometers. *Atmospheric Measurement Techniques*, 9(8), 3769–3791. <https://doi.org/10.5194/amt-9-3769-2016>
- Liljegren, J. C., Clothiaux, E. E., Mace, G. G., Kato, S., & Dong, X. (2001). A new retrieval for cloud liquid water path using a ground-based microwave radiometer and measurements of cloud temperature. *Journal of Geophysical Research*, 106(D13), 14,485–14,500. <https://doi.org/10.1029/2000JD900817>
- Luke, E. P., & Kollias, P. (2013). Separating cloud and drizzle radar moments during precipitation onset using Doppler spectra. *Journal of Atmospheric and Oceanic Technology*, 30(8), 1656–1671. <https://doi.org/10.1175/JTECH-D-11-00195.1>
- Malinowski, S. P., Gerber, H., Jen-La Plante, I., Kopec, M. K., Kumala, W., Nurowska, K., et al. (2013). Physics of stratocumulus top (POST): Turbulent mixing across capping inversion. *Atmospheric Chemistry and Physics*, 13(24), 12,171–12,186. <https://doi.org/10.5194/acp-13-12171-2013>
- Morcrette, J.-J., Mlawer, E. J., Iacono, M. J., & Clough, S. A. (2001). Impact of the radiation-transfer scheme RRTM in the ECMWF forecasting system. *ECMWF Newsletter*, No. 91, ECMWF, Reading, United Kingdom, 2–9. Retrieved from <http://www.ecmwf.int/sites/default/files/elibrary/2001/14633-newsletter-no91-summer-2001.pdf>
- Morrison, H., & Gettelman, A. (2008). A new two-moment bulk stratiform cloud microphysics scheme in the Community Atmosphere Model, version 3 (CAM3), Part I: Description and numerical tests. *Journal of Climate*, 21(15), 3642–3659. <https://doi.org/10.1175/2008JCLI2105.1>
- O'Connor, E. J., Hogan, R. J., & Illingworth, A. J. (2005). Retrieving stratocumulus drizzle parameters using doppler radar and lidar. *Journal of Applied Meteorology*, 44(1), 14–27. <https://doi.org/10.1175/JAM-2181.1>
- O'Connor, E. J., Illingworth, A. J., & Hogan, R. J. (2004). A technique for autocorrelation of cloud lidar. *Journal of Atmospheric and Oceanic Technology*, 21(5), 777–786. [https://doi.org/10.1175/1520-0426\(2004\)021<0777:ATFAOC>2.0.CO;2](https://doi.org/10.1175/1520-0426(2004)021<0777:ATFAOC>2.0.CO;2)
- Rapp, A. D. (2016). Observational evidence linking precipitation and mesoscale cloud fraction in the southeast Pacific. *Geophysical Research Letters*, 43, 7267–7273. <https://doi.org/10.1002/2016GL069906>
- Sharon, T. M., Albrecht, B. A., Jonsson, H. H., Minnis, P., Khaiyer, M. M., van Reken, T. M., et al. (2006). Aerosol and cloud microphysical characteristics of rifts and gradients in maritime stratocumulus clouds. *Journal of the Atmospheric Sciences*, 63(3), 983–997. <https://doi.org/10.1175/JAS3667.1>
- Stevens, B., Lenschow, D. H., Faloona, I., Moeng, C., Lilly, D. K., Blomquist, B., et al. (2003). On entrainment rates in nocturnal marine stratocumulus. *Quarterly Journal of the Royal Meteorological Society*, 129(595), 3469–3493. <https://doi.org/10.1256/qj.02.202>
- Stevens, B., Lenschow, D. H., Vali, G., Gerber, H., Bandy, A., Blomquist, B., et al. (2003). Dynamics and chemistry of marine stratocumulus —DYCOMS-II. *Bulletin of the American Meteorological Society*, 84(5), 579–594. <https://doi.org/10.1175/BAMS-84-5-579>
- Stevens, B., Vali, G., Comstock, K., Wood, R., van Zanten, M. C., Austin, P. H., et al. (2005). Pockets of open cells and drizzle in marine stratocumulus. *Bulletin of the American Meteorological Society*, 86(1), 51–58. <https://doi.org/10.1175/BAMS-86-1-51>
- Testud, J., Oury, S., Black, R. A., Amayenc, P., & Dou, X. (2001). The concept of “normalized” distribution to describe raindrop spectra: A tool for cloud physics and cloud remote sensing. *Journal of Applied Meteorology*, 40(6), 1118–1140. [https://doi.org/10.1175/1520-0450\(2001\)040<1118:TCONDNT>2.0.CO;2](https://doi.org/10.1175/1520-0450(2001)040<1118:TCONDNT>2.0.CO;2)

- Toto, T., & Jensen, M. (2016). Interpolated sounding and gridded sounding value-added products. Ed. by Robert Stafford, ARM Climate Research Facility. *DOE/SC-ARM-TR-183*
- Wilbanks, M. C., Yuter, S. E., De Szoeke, S. P., Brewer, W. A., Miller, M. A., Hall, A. M., & Burleyon, C. D. (2015). Near-surface density currents observed in the Southeast Pacific stratocumulus-topped marine boundary layer. *Monthly Weather Review*, *143*(9), 3532–3555. <https://doi.org/10.1175/MWR-D-14-00359.1>
- Wiscombe, W. J. (1988). Improved Mie scattering algorithms. *Applied Optics*, *19*, 1505–1509. <https://doi.org/10.1364/AO.19.001505>
- Wood, R. (2005). Drizzle in stratiform boundary layer clouds. Part I: Vertical and horizontal structure. *Journal of the Atmospheric Sciences*, *62*(9), 3011–3033. <https://doi.org/10.1175/JAS3529.1>
- Wood, R. (2012). Stratocumulus Clouds. *Monthly Weather Review*, *140*(8), 2373–2423. <https://doi.org/10.1175/MWR-D-11-00121.1>
- Wood, R., & Hartmann, D. L. (2006). Spatial variability of liquid water path in marine low cloud: The importance of mesoscale cellular convection. *Journal of Climate*, *19*(9), 1748–1764. <https://doi.org/10.1175/JCLI3702.1>
- Wood, R., Jensen, M. P., Wang, J., Bretherton, C. S., Burrows, S. M., Del Genio, A. D., et al. (2016). Planning the next decade of coordinated research to better understand and simulate marine low clouds. *Bulletin of the American Meteorological Society*, *97*(9), 1699–1702. <https://doi.org/10.1175/BAMS-D-16-0160.1>
- Wood, R., Wyant, M., Bretherton, C. S., Rémillard, J., Kollias, P., Fletcher, J., et al. (2015). Clouds, aerosols, and precipitation in the marine boundary layer: An ARM mobile facility deployment. *Bulletin of the American Meteorological Society*, *96*(3), 419–440. <https://doi.org/10.1175/BAMS-D-13-00180.1>
- Yamaguchi, T., Feingold, G., & Kazil, J. (2017). Stratocumulus to cumulus transition by drizzle. *Journal of Advances in Modeling Earth Systems*, *9*, 2333–2349. <https://doi.org/10.1002/2017MS001104>
- Yang, F., Luke, E. P., Kollias, P., Kostinski, A. B., & Vogelmann, A. M. (2018). Scaling of drizzle virga depth with cloud thickness for marine stratocumulus clouds. *Geophysical Research Letters*, *45*(8), 3746–3753. <https://doi.org/10.1029/2018GL077145>
- Zheng, X., Klein, S. A., Ma, H.-Y., Bogenschutz, P., Gettelman, A., & Larson, V. E. (2016). Assessment of marine boundary layer cloud simulations in the CAM with CLUBB and updated microphysics scheme based on ARM observations from the Azores. *Journal of Geophysical Research: Atmospheres*, *121*, 8472–8492. <https://doi.org/10.1002/2016JD025274.29>
- Zheng, X., Klein, S. A., Ma, H.-Y., Caldwell, P., Larson, V. E., Gettelman, A., & Bogenschutz, P. (2017). A cloudy planetary boundary layer oscillation arising from the coupling of turbulence with precipitation in climate simulations. *Journal of Advances in Modeling Earth Systems*, *9*, 1973–1993. <https://doi.org/10.1002/2017MS000993>
- Zhou, X., Kollias, P., & Lewis, E. R. (2015). Clouds, precipitation, and marine boundary layer structure during the MAGIC field campaign. *Journal of Climate*, *28*(6), 2420–2442. <https://doi.org/10.1175/JCLI-D-14-00320.1>